Published in final edited form as:

J Control Release. 2020 January 10; 317: 259–272. doi:10.1016/j.jconrel.2019.11.032.

Ginsenoside Rg3-loaded, reactive oxygen species-responsive polymeric nanoparticles for alleviating myocardial ischemia-reperfusion injury

Lan Li[a,b,1], **Yili Wang**[a,b,1], **Rui Guo**[a,b], **Sheng Li**[a,b], **Jingyu Ni**[a,b], **Shan Gao**[a,b], **Xiumei Gao**[b], **Jingyuan Mao**[a], **Yan Zhu**[b], **Pingli Wu**[c], **Hongjun Wang**[d], **Deling Kong**[c], **Han Zhang**[b], **Meifeng Zhu**[c,d,*], **Guanwei Fan**[a,b]

[a]First Teaching Hospital of Tianjin University of Traditional Chinese Medicine, Tianjin 300193, China

[b]Tianjin Key Laboratory of Translational Research of TCM Prescription and Syndrome, Tianjin University of Traditional Chinese Medicine, Tianjin 301617, China

[c]College of Life Sciences, Key Laboratory of Bioactive Materials (Ministry of Education), State Key Laboratory of Medicinal Chemical Biology, Xu Rongxiang Regeneration Life Science Center, Nankai University, Tianjin 300071, China

[d]Department of Biomedical Engineering, Stevens Institute of Technology, Hoboken, NJ 07030, USA

Abstract

Myocardial ischemia-reperfusion injury (MIRI) is a serious threat to the health and lives of patients without any effective therapy. Excessive production of reactive oxygen species (ROS) is considered a principal cause of MIRI. Some natural products, including ginsenoside Rg3 (Rg3), exhibit robust antioxidant activity. However, the lack of an effective delivery strategy for this hydrophobic compound hinders its clinical application. In addition, therapeutic targets and molecular mechanisms of Rg3 require further elucidation to establish its mode of action. This study aimed to generate ROS-responsive nanoparticles (PEG-b-PPS) *via* the self-assembly of diblock copolymers of poly (ethylene glycol) (PEG) and poly (propylene sulfide) (PPS) and use them for Rg3 encapsulation and delivery. We identified FoxO3a as the therapeutic target of Rg3 using molecular docking and gene silencing. In rat ischemia-reperfusion model, an intramyocardial injection of Rg3~loaded PEG-b-PPS nanoparticles improved the cardiac function and reduced the infarct size. The mechanism of action was established as Rg3 targeting of FoxO3a, which inhibited the promotion of oxidative stress, inflammation, and fibrosis *via* downstream signaling pathways. In conclusion, this approach, involving ROS-responsive drug release, together with the identification of the target and mechanism of action of Rg3, provided an

---

[*] Corresponding authors. zhanghan@tjutcm.edu.cn (H. Zhang), zhumeifeng2013@163.com (M. Zhu), guanwei.fan@tjutcm.edu.cn (G. Fan).

[1] Co-frist author.

Appendix A. Supplementary data

Supplementary data to this article can be found online at https://doi.org/10.1016/j.jconrel.2019.11.032

effective strategy for treating ischemic diseases and oxidative stress and could accelerate the implementation of hydrophobic natural products in clinical applications.

Keywords

FoxO3a; Ginsenoside Rg3; Myocardial ischemia-reperfusion injury; ROS-responsive nanoparticles

1. Introduction

Acute myocardial infarction (AMI) is the leading cause of morbidity and mortality worldwide. Reperfusion following thrombolytic or primary percutaneous coronary intervention is considered to be the most effective treatment [1,2]. However, an incidence of 10%–25% of recurrent AMI and a hospital mortality rate of 6%–14% in patients with myocardial ischemia-reperfusion injury (MIRI) has been reported [3,4]. Potential mechanisms for MIRI include inflammation, energy metabolism disorder, oxidative stress, and apoptosis [5]. Oxidative stress is considered a primary contributory factor in the pathogenesis of MIRI. Accumulation of reactive oxygen species (ROS) causes a variety of injuries, including mitochondrial damage and myocardial apoptosis [6]. Therefore, designing an ROS-responsive release system would be beneficial in improving the therapeutic efficacy of drugs [7,8]. In addition, finding an appropriate drug target and defining the therapeutic mechanisms of action of drugs used to treat MIRI has important value for clinical and scientific research. However, the development of an effective, mechanism-targeted approach to treat MIRI remains to be solved.

Large numbers of natural products exhibit anti-oxidative effects *in vitro* and *in vivo* [9]. Ginsenoside Rg3 (Rg3), the main active ingredient of ginseng, has a range of pharmacological effects, including antioxidant, anti-inflammatory, and anti-aging activities [10–13]. Our previous studies confirmed that Rg3-loaded Pluronic F127 micelles alleviated doxorubicin-induced oxidative stress by reversing mitochondrial dysfunction [14]. In addition, Rg3 enhanced the effect of MIRI treatment by regulating the AKT/nitric oxide synthase pathway [15,16]. However, the specific target and the molecular mechanism of action of Rg3 in treating MIRI remain unclear. In addition, the mode of loading hydrophobic Rg3 can affect its targeting and the responsiveness of injured tissues, thus inhibiting its therapeutic effect on MIRI.

The micelles formed from amphiphilic block copolymers have shown promise as carriers for the delivery of hydrophobic drugs [17,18]. Poly (ethylene glycol) (PEG) is usually used as the hydrophilic block due to its resistance to protein adsorption and low toxicity. Poly (propylene sulfide) (PPS) can be chosen as the hydrophobic block owing to its extreme hydrophobicity [19]. In response to ROS, PPS is oxidatively converted from a hydrophobe into a hydrophile [19,20]. Such a PEG-b-PPS amphiphilic block copolymer can be used as an ROS-responsive nanovesicle for drug delivery [21,22]. Melatonin (Mel) released from ROS-responsive Mel-loaded PEG-b-PPS reduces sepsis-induced acute liver injury [23], suggesting that the use of PEG-b-PPS to encapsulate Rg3 may facilitate the release of Rg3 at ROS-generating sites, thus improving the treatment of MIRI.

In the present study, self-assembled ROS-responsive polymers of PEG and PPS diblock copolymers were prepared for the encapsulation of Rg3. The physical structural parameters of Rg3-loaded nanoparticles and their ROS-responsive release behavior *in vitro* and *in vivo* were investigated. The administration of intramyocardial injections of the Rg3-loaded, ROS-responsive polymeric nanoparticles (PEG-b-PPS-Rg3) into rats with MIRI showed an improved myocardial therapeutic effect. Furthermore, by molecular docking and gene silencing, FoxO3a was identified as a specific and effective target for Rg3. The released Rg3 activated FoxO3a, which had anti-oxidative, anti-inflammatory, and anti-fibrotic functions. In short, the use of ROS-responsive nanoparticles and the exploration of therapeutic targets and mechanisms of Rg3 may provide a new strategy for treating MIRI, leading to the clinical application of Rg3.

2. Materials and methods

2.1 Materials

Poly (ethylene glycol) (mPEG, Mn = 2.0×10^3 g/mol), propylene sulfide, hydrogen peroxide (H_2O_2), thioacetic acid, methacryloyl chloride, polyvinyl alcohol, and trimethylamine were obtained from GL Biochem Co., Ltd. (Shanghai, China). All the solvents were obtained from Sigma-Aldrich China Inc. (Shanghai, China). 3,3′-Dioctadecyloxacarbocyanine perchlorate (DiO), 1,1′-dioctadecyl-3,3,3′,3′-tetramethylindocarbocyanine perchlorate (DiI), dihydroethidium (DHE), 2′,7′-dichlorofluorescin diacetate (DCFH-DA), tetrechloro-tetraethylbenzimidazol carbocyanine iodide (JC-1), MitoTracker Green fluorescent probe (MitoTracker), and 4′,6-diami-dino-2-phenylindole (DAPI) were obtained from Beyotime Biotechnology Co., Ltd. (Beijing, China). Rg3 was obtained from Shanghai Winherb Medical Technology Co., Ltd. (Shanghai, China). 3-(4, 5-dimethylthiazol-2-yl)-2, 5-diphenyltetrazolium bromide (MTT) and 2,3,5-triphenyl-2H-tetrazolium chloride (TTC) were obtained from Solarbio life sciences Co., Ltd. (Beijing, China). The enzyme-linked immunosorbent assay (ELISA) kits, including dismutase (SOD), malondialdehyde (MDA), interleukin (IL)-6 and IL-1β, tumor necrosis factor-α (TNF-α), and C-reactive protein (CRP), were obtained from Wuhan Cloud-Clone Inc. (Wuhan, China). Terminal dUTP nick end-labeling (TUNEL) assays kit was obtained from Roche Life Science (USA). ROS Elisa Kit was obtained from DuMa biological Co., Ltd. (Shanghai, China). Caspase-Glo 3/7 assay kit was obtained from Thermo Scientific China Inc. (Shanghai, China). All the antibodies were obtained from Abcam China Inc. (Shanghai, China). Male Sprague-Dawley (SD) rats (8 weeks old) were purchased from Beijing Vital River Laboratory Animal Technology Co., Ltd. (Beijing, China).

2.2. Preparation and characterization of PEG-b-PPS

PEG-b-PPS was prepared as described in a previous study [23]: (1) First, 0.5 mmol of mPEG, 0.6 mmol of methacryloyl chloride and 0.6 mL of trimethylamine were added to dichloromethane. The preparation was stirred for 24 h, and the solution was filtered and concentrated, and the solids were precipitated twice using cold diethyl ether. (2) Next, 0.5 mmol of the obtained preparation, 0.187 mmol of 2, 2-azobisisobutyronitrile, and 7.6 mmol of thioacetic acid were dissolved in 8 mL of tetrahydrofuran (THF) with stirring. The reaction mixture was cooled with liquid nitrogen, degassed by applying vacuum, and then returned to room temperature. The degassing procedure was repeated three times. After stirring at 60 °C for 24 h, the reaction mixture was filtered, concentrated, and precipitated twice using cold diethyl ether. (3) Further, 0.5 mmol of the solution obtained from step 2 and 0.6 mmol of sodium methylate were dissolved in 8 mL of THF with stirring for 30 min at 25 °C. Then, 30 mmol of propylene sulfide was added to the mixture, and the solution was maintained at 60 °C overnight with constant stirring. The solvent was then removed, and the viscous liquid was extracted twice with methanol and characterized by ^{1}H nuclear magnetic resonance (NMR) spectroscopy (Agilent, USA). The average molecular weight of PEG-b-PPS was characterized by gel permeation chromatography (GPC).

2.3. Rg3-loaded PEG-b-PPS nanoparticles (PEG-b-PPS-Rg3) preparation and characterization

Rg3 (10 mg) was dissolved into 200 μL of 0.9% saline (0.1538 mol/L)/ethanol (1:1, *v:v*) and PEG-b-PPS (16 mg) in 1 mL of chloroform. The solution was emulsified by sonication for 3 min (70 W). Then, 4 mL of saline with 0.5% (*w/v*) of polyvinyl alcohol was slowly added, and the preparation was further emulsified by sonication for 60 s (200 W). Ethanol and chloroform were removed from the final emulsion using a rotary evaporator at 40 °C. The particle sizes of PEG-b-PPS-Rg3 and blank PEG-b-PPS were detected by dynamic light scattering after diluting them to a final concentration of 1 mg/mL with deionized water. The mean size and polydispersity index for three replicates were measured. The morphology of PEG-b-PPS-Rg3 was characterized by transmission electron microscopy (TEM, EM-200CX, JEOL Ltd., Tokyo, Japan). Encapsulation ratios (ER %) and drug-loading efficiency (DL %) was calculated using the following equations:

$$\mathrm{ER}\% = \frac{Weight\ of\ the\ drug\ in\ micelles}{Weight\ of\ the\ feeding\ drug} \times 100\%$$

$$\mathrm{DL}\% = \frac{Weight\ of\ the\ drug\ in\ micelles}{Weight\ of\ the\ feeding\ polymer\ and\ drug} \times 100\%$$

2.4. MIRI model preparation and drug administration

The SD rats were fasted for 12 h before use in experiments but were allowed free access to water. The experimental procedures conformed to the Directive 2010/63/EU of the European Parliament, and all animals were handled according to the guidelines of the TCM Animal Research Committee (TCM-LAEC2014005) of Tianjin University. All rats were randomly divided into four groups: (1) sham (n = 10, 100 μL PBS), (2) model (*n* = 10, 100 μL PBS), (3) PEG-b-PPS (*n* = 10, 100 μL PEG-b-PPS), and (4) PEG-b-PPS-Rg3 (*n* = 10, 100 μL PEG-b-PPS-Rg3 containing 0.5 mg Rg3). For an ischemia-reperfusion (I/R) model [24], the rats were anesthetized with an intraperitoneal injection of 5% chloral hydrate (30 mg/kg), and thoracotomies were performed at the fourth intercostal space to expose the heart. A 6–0 silk suture was used to ligate the left anterior descending coronary artery. After 30 min, the suture was removed to allow for reperfusion. The sham group underwent the same procedure without ligation. For the PEG-b-PPS-Rg3 group, PEG-b-PPS-Rg3 was administered *via* a single intramyocardial injection at the time of ligation. For the PEG-b-PPS group, equal amounts of PEG-b-PPS were administered. The rats in the sham and model groups were intramyocardially injected with 100 μL of PBS.

2.5. Stability and ROS-responsive studies

We evaluated ROS-responsive studies using 0, 0.01, 0.05, 0.1, and 1 mM H_2O_2 to assess the *in vitro* release behavior. Dialysis tube (MWCO = 1000 Da) was used to collect free Rg3. Dialysis tube containing 1 mL of freshly prepared PEG-b-PPS-Rg3 was dispersed into 50 mL 0.2 M phosphate buffer (pH 7.4) with 0, 0.01, 0.05, 0.1, and 1 mM H_2O_2 at 37 °C. Subsequently, 2 mL of the solutions was withdrawn at 0, 1, 2, 3, 4, 6, 12, 24, 36, 48, and 72 h. Then, 2 mL fresh PBS was added. The collected samples were diluted with methanol (volume ratio, 1:1) and quantified by high-performance liquid chromatography (HPLC). Briefly, the concentrations of Rg3 were determined by HPLC with detection at the λ max (203 nm) and a retention time of 9.23 min.

2.6. Fluorescence resonance energy transfer used for detecting ROS response in vivo

Fluorescence resonance energy transfer (FRET) was used to investigate the disassembly of the PEG-b-PPS in response to ROS [23,25–27]. DiO and DiI were loaded based on the procedure used for Rg3 loading described earlier, which served as the FRET donor and acceptor, respectively, to test the on-demand release of PEG-b-PPS. DiO (1 mg/kg rat weight) and DiI (1 mg/kg rat weight)-loaded PEG-b-PPS were dissolved in 100 μL of PBS and then administered *via* a single intramyocardial injection before MIRI. After 2 h of reperfusion, fluorescence images of the hearts were acquired using IVIS Kinetic.

2.7. Echocardiographic assessment of left ventricular function

A Vevo 2100 (VisualSonic, Canada) ultra-high-resolution animal ultrasound imaging system was used to evaluate the left ventricular function, asdescribed [14]. The following parameters were measured as the indicators of function: systolic interventricular septum (IVS_s), diastolic interventricular septum (IVS_d), systolic left ventricular posterior wall ($LVPW_s$), diastolic left ventricular posterior wall ($LVPW_d$), left ventricular systolic diameter ($IVID_s$), left ventricular diastolic diameter ($IVID_d$), left ventricular systolic volume ($LVVol_s$), left ventricular diastolic volume ($LVVol_d$), ejection fraction (EF%), fractional shortening (FS%), aortic valve peak velocity, and aortic valve peak pressure.

2.8. 2,3,5-Triphenyltetrazolium chloride staining (TTC staining) analysis

After 2 h reperfusion, the rats were euthanized. The hearts were harvested, cut into six transverse slices on average, and incubated with TTC (1% solution in PBS) for 30 min at 37 °C in the dark. Then, the transverse slices were washed with PBS three times and subsequently imaged. The infarcted myocardium was stained in white, and the viable tissue was stained in red color, and then analyzed using ImageJ software (MD, USA) as reported in a previous study [24].

$$percentage\ of\ Infarct\ size = (\text{Infarct size/Viable size}) \times 100\%$$

2.9 Plasma biochemistry and enzyme-linked immunosorbent assay

Plasma biochemistry, including creatine kinase (CK), creatine kinase-MB (CK-MB), and lactate dehydrogenase (LDH), was assessed using an auto-analyzer (Multiskan MK3; Thermo Fisher Scientific, USA). The plasma levels of SOD, MDA, IL-6, IL-Iβ, TNF-α, and CRP were determined using the ELISA kits according to the manufacturer's protocol as reported in a previous study [14].

2.10. Histological analysis

The heart tissues were fixed using 4% paraformaldehyde for 48 h. The tissues were embedded in paraffin, cut into 4 pM sections, and subjected to hematoxylin/eosin staining (H&E) and Sirius red (SR). TUNEL assays were performed in accordance with the manufacturer's protocol. The Sections in 5 mM DHE or 10 μM DCFH-DA were incubated for 15–25 min in the dark. After washing with PBS, they were stained using 0.5 μg/mL DAPI. For immunofluorescence (IF) analysis, sections were incubated with TNF-α (1:200 dilution) at 4 °C for 12 h and subsequently incubated with anti-rat HRP(Alexa Fluor 647) at 37 °C for 1 h. After washing with PBS, the sections were counterstained with the DAPI. The sections were examined using a fluorescence microscope and a digital camera (Carl Zeiss, Axio Observer Al).

2.11. Measurement of ROS content in the heart

The hearts from rats were homogenized in 1 mL of PBS at 4 °C. Then, 100 μL of heart homogenate was used for determining the ROS content. The ROS content was measured using ROS Elisa Kit in accordance with the manufacturer's protocol.

2.12. Cell transfection

Viruses carrying FoxO3a shRNA or their vector controls were produced by transfecting HEK293T cells with viral packaging vectors (psPAX2, pMD2G), using a standard calcium phosphate transfection method. The viruses were harvested from the supernatant of HEK293T cells 48 h after transfection before being used to infect H9C2 cells.

2.13. Hypoxia/reoxygenation injury analysis

Hypoxia/reoxygenation (H/R) was performed with H9C2 cells to simulate I/R injury. After treatment with 10 nM Rg3 for 24 h, H/R was simulated as described in a previous study [28]. Briefly, the cultured H9C2 cells were placed in a hypoxia chamber (StemCell Technologies, CA, USA) with glucose-free DMEM (pH 6.8). The chamber was flushed with 95% (*v/v*) N_2 and 5% (*v/v*) CO_2 with a flow rate of 15 L/min for 10 min at 37 °C. After 6 h of hypoxia, reoxygenation was accomplished by replacing the medium with DMEM containing 4.5 mM glucose (pH 7.4) and subsequent incubation in a CO_2 incubator [5% (*v/v*) CO_2–95% (*v/v*) O_2] for 18 h. The cell viability was assessed with MTT according to the manufacturer's protocol. For the Caspase-Glo 3/7 assay, the cells were seeded in opaque 96-well plates, and luminescence was measured following the manufacturer's protocol. The ROS levels were measured using DCFH-DA, and the fluorescence was excited at 488 nm and collected at 525 nm. Mitochondrial inner membrane potential ($\Delta\Psi_m$) was checked using JC-1 and MitoTracker. The cells displayed red fluorescence when the mitochondrial membrane retained integrity. Moreover, the cells showed green fluorescence when the mitochondrial membrane was damaged. Fluorescent images of ROS and JC-1 were observed using a fluorescence microscope and a digital camera as described previously (Carl Zeiss, Axio Observer A1) [29,30].

2.14. Automated Western blot analysis

The Western blot analysis was performed on a Peggy Sue automated system (ProteinSimple, USA) according to the manufacturer's protocol using a Size Separation Master Kit with split buffer (12–230 kDa). The primary antibodies used were FoxO3a, Sirt1, PGC-1α, Nrf1, Nrf2, HO-1, SOD1, P65-NFκB, P-IKBα, TGF-β, Smad2, P-Smad2, Smad3, P-Smad3, MMP2, MMP9, BAX, and Bcl-2. The quantification of Western blots was accomplished using the ProteinSimple software, version 2.7.1.

2.15. Molecular docking

Molecular docking was performed using Autodock Vina 1.1.2 to investigate the binding between ginsenoside Rg3 and human FoxO3a [31]. The three-dimensional (3D) structure of FoxO3a (PDB ID: 2UZK) was downloaded from the RCSB Protein Data Bank (http://www.rcsb.org/). The 2D structure of Rg3, drawn using ChemBioDraw Ultra 14.0, was converted into a 3D structure using the ChemBio3D Ultra 14.0 software. The AutoDockTools 1.5.6 package [32,33] was employed to generate the docking input files. The ligand was prepared for docking by merging nonpolar hydrogen atoms and defining rotatable bonds. The value of exhaustiveness was set to 20 to increase the docking accuracy. For Vina docking, the default parameters were used. The best-scoring pose, as assessed using the Vina docking score, was chosen and visually analyzed using the PyMoL 1.7.6 software (http://www.pymol.org/).

2.16. Statistical analyses

The data were presented as means ± standard deviation. Statistical analyses were performed using SAS statistical software (SAS Institute Inc., NC, USA). Differences between groups were compared using analysis of variance with Student–Newman–Keuls *post hoc* test for multiple comparisons when the normality and homogeneity of the variance assumptions were satisfied. A P value < .05 was considered statistically significant.

3. Results

3.1. Characterization and responsive release of PEG-b-PPS-Rg3 nanoparticles

The physical structural parameters of PEG-b-PPS-Rg3 nanoparticles and their release behavior *in vitro* and *in vivo* were characterized to prove encapsulation efficiency. GPC were used to detect the average molecular weights (MW) of the block copolymers PEG-b-PPS, which is approximate 7.6 KD. ER% and DL% of PEG-b-PPS-Rg3 were 87.29% ± 3.12% and 31.33% ± 1.72%, respectively. The peaks in the ^{1}H NMR spectrum showed the effectiveness of the PEG-b-PPS diblock polymerization (Fig. 1A). The average hydrodynamic diameter of the PEG-b-PPS-Rg3 was close to that of PEG-b-PPS, and both showed a uniform size distribution (Fig. 1B). The appearance of PEG-b-PPS-Rg3 did not differ appreciably compared with that for PEG-b-PPS (Fig. 1C). TEM results showed that the morphology changes from a smooth to a rough surface after loading Rg3 (PEG-b-PPS-Rg3) (Fig. 1D). A large amount of ROS composed of superoxide anion ($O_2 - \cdot$). hydroxyl radicals (OH –), and H_2O_2 [34], was generated during MIRI. Since $O_2 - \cdot$ and OH– are chemically unstable, H_2O_2 of different concentrations was used to simulate the disassembly of the PEG-b-PPS in response to ROS *in vitro* (Fig. 1E). The Rg3 release rate for PEG-b-PPS-Rg3 was enhanced in the presence of H_2O_2 (Fig. 1E). In 72 h, 32.63% ± 1.25%, 42.61% ± 2.22%, 61.70% ± 3.32%, and 80.44% ± 2.27% of Rg3 was released in the presence of 0.01, 0.05, 0.1, and 1 mM H_2O_2, respectively, which were significantly higher than that in the absence of H_2O_2 (18.99% ± 1.28%). This result also verified that PEG-b-PPS-Rg3 had respectable stability in PBS (Fig. 1E). The *in vivo* release behavior of PEG-b-PPS was measured using FRET after administering PEG-b-PPS co-loaded with DiO and DiI to sham or model rats (Fig. 1F, G). FRET signal (emission DiI, upon excitation of DiO) appeared only when DiO and DiI were co-loaded into PEG-b-PPS. *Ex vivo* fluorescence imaging indicated a significant reduction in the FRET signal in the heart of model rats compared to the Sham rats, representing that release of DiO and DiI from the PEG-b-PPS was dependent on generation of excess ROS in heart by I/R (Fig. 1F and Fig. S1A). FRET signal quantified using total radiation efficiency further confirmed this tendency (Fig. 1G). These results displayed that the PEG-b-PPS-Rg3 encapsulation system was appropriately prepared and it responded to ROS *in vivo* and *in vitro.*

3.2. Rg3 exerted anti-oxidative stress effects by binding to FoxO3a

Molecular docking was used to screen for the therapeutic targets of Rg3, and the results were verified using gene knockdown at the cellular level. Rg3 docked into the binding site of FoxO3a (Fig. 2A, B). The maximum binding affinity between Rg3 and FoxO3a was predicted to be −6.0 kcal/mol. Rg3 adopted a compact conformation to bind to FoxO3a (Fig. 2A). The aglucone of Rg3 was located at the hydrophobic pocket, surrounded by the residues Pro-174, Leu-178, Trp-186, and Cys-190, forming a strong hydrophobic bond (Fig. 2B). Four key hydrogen bond interactions were evident between Rg3 and the residues Thr-179 (bond length: 2.7 Å), Gln-182 (bond length: 2.2 Å), and Lys-230 (bond lengths: 1.9 Å and 2.4 Å), which provided the main interaction between Rg3 and FoxO3a (Fig. 2B). FoxO3a shRNA adenovirus was used to knockdown FoxO3a in H9C2 cells to verify this hypothesis, and the intervention effect of Rg3 was evaluated. The activity of H9C2 cells decreased after H/R injury and increased when Rg3 was added. However, the activity of H9C2 cells in the H/R injury was not elevated by adding Rg3 after the knockdown of FoxO3a, indicating a direct interaction between Rg3 and FoxO3a (Fig. 2C). The activity of caspase 3/7 was used to evaluate the effect of Rg3 on H/R-induced apoptosis. The activity of caspase 3/7 in H/R group was elevated compared with that in the control group, and decreased after Rg3 treatment, but it exhibited no obvious change after the knockdown FoxO3a (Fig. 2D). H/R injury was associated with ROS generation and mitochondrial depolarization (the $\Delta\Psi_m$ decrease) [35]. The ROS fluorescence staining showed that Rg3 significantly reduced the ROS level in H9C2 cells induced by H/R, but the effect disappeared after the knockdown of FoxO3a (Fig. 2E, F). $\Delta\Psi_m$ was checked using JC-1 and MitoTracker. The JC-1 accumulates in healthy mitochondria as aggregates displaying red fluorescence, while in depolarized or damaged mitochondria, JC-1 transforms into monomers exhibiting green fluorescence. JC-1 fluorescence staining exhibited that the $\Delta\Psi_m$

of H9C2 cells in H/R group was decreased compared with that in the control group and recovered after Rg3 treatment but showed no apparent variation after the knockdown of FoxO3a (Fig. 2G). The quantitative results (red fluorescence/green fluorescence) were consistent with the results of JC-1 staining (Fig. 2H). MitoTracker showed the same trend (Fig. 2I). The Western blot analysis results showed that the expression of FoxO3a could not be detected after FoxO3a knockdown (Fig. 2J); the expression of oxidative stress-related proteins, including Sirtl, PGC-1α, and SOD1 decreased after H/R injury; Rg3 enhanced the expression of these proteins compared with that in the H/R group. However, the expression of oxidative stress-relate proteins was not increased by Rg3 treatment after the knockdown of FoxO3a (Fig. 2J and Fig. S2A–S2D). Subsequently, the protective effect of PEG-b-PPS-Rg3 on H/R injury was evaluated. PEG-b-PPS-Rg3 also reduced ROS production (Fig. 2K, and Fig. S2E) and increased H9C2 cell viability (Fig. 2L) compared with the H/R group, and protective effect disappeared after the knockdown of FoxO3a. PEG-b-PPS has no therapeutic effect (Fig. 2 L). The aforementioned results showed that Rg3 released from PEG-b-PPS-Rg3 targeted FoxO3a to inhibit oxidative stress damage caused by H/R.

3.3. ROS-responsive PEG-b-PPS-Rg3 nanoparticles attenuated myocardial infarction

The I/R rat model was used to evaluate the response of PEG-b-PPS-Rg3 to ROS and their therapeutic effect on MIRI. PEG-b-PPS-Rg3 (2.5 mg/kg Rg3 of rat weight) was injected directly into the heart of rats (Fig. 3). High mortality caused by the direct intramyocardial injection of free Rg3 demonstrated that Rg3 could not be used for direct intramyocardial injection (Fig. S1B). This result also confirmed that the application of PEG-b-PPS-Rg3 for intramyocardial injection will be necessary. The myocardial infarct size was assessed by TTC staining. The model group exhibited severe myocardial infarction (Fig. 3A, B). The myocardial infarction area reduced after the intramyocardial injection of PEG-b-PPS-Rg3, while the PEG-b-PPS group showed no appreciable reduction (Fig. 3A, B). Intensity of DHE fluorescence and DCFH-DA fluorescence was stronger in tissues of model group compared with those of sham group, indicating that the myocardium was exposed to high levels of ROS during I/R (Fig. 3C, D, and Fig. S3A, S3B). The fluorescence intensity in the PEG-b-PPS-Rg3 group was lower than that in the model and PEG-b-PPS group, indicating that PEG-b-PPS-Rg3 was able to decrease the generation of ROS. Indeed, the intensity of fluorescence also tended to decrease in PEG-b-PPS group but with no statistical difference.

3.4. PEG-b-PPS-Rg3 nanoparticles improved cardiac function against MIRI

The effects of PEG-b-PPS-Rg3 on cardiac functions were assessed by echocardiography. As shown by the M-mode echocardiograms (Fig. 4A), the left ventricular contraction movement was attenuated in the model group. Compared with the model group, the amplitude of the left ventricular wall motion was stronger after the intramyocardial injection of PEG-b-PPS-Rg3 but showed no apparent improvement in the PEG-b-PPS group. EF% and FS% were enhanced in the PEG-b-PPS-Rg3 group compared with the model group, indicating that PEG-b-PPS-Rg3 could improve cardiac function after I/R (Fig. 4B, C). Moreover, IVS_s, IVS_d, $LVPW_s$, and $LVPW_d$ decreased (Fig. S4A, S4C, S2E, and S4G) and $IVID_s$, $IVID_d$, $LVVol_s$, and $LVVol_d$ (Fig. S4B, S4D, S4F, and S4H) increased in the model group, indicating ventricular dilation after I/R. After the intramyocardial injection of PEG-b-PPS-Rg3, ventricular dilation of I/R rats was inhibited. Aortic blood flow was assessed using color Doppler ultrasound. As the diameter of the aortic outflow tract showing no obvious difference among four groups, PEG-b-PPS-Rg3 enhanced the velocity and pressure of aortic blood flow compared with the model group (Fig. 4D, E, and Fig. S4I, S4J). H&E staining revealed that the degrees of inflammatory cell infiltration, edema, and architecture disruption were enhanced in the model (Fig. 4F). After the intramyocardial injection of PEG-b-PPS-Rg3, the degree of myocardium injury was less extensive (Fig. 4F). The levels of CK, CK-MB, and LDH negatively correlated with cardiac functions [36]. The serum levels of these factors were higher in the model group compared with the sham group. And these levels decreased after PEG-b-PPS-Rg3 injections (Fig. 4G–I). In this study, the PEG-b-PPS group showed no obvious effect in improving cardiac function. These results indicated that PEG-b-PPS-Rg3 protected cardiac functions against MIRI.

3.5. PEG-b-PPS-Rg3 nanoparticles exerted an anti-oxidative effect in rats with MIRI

The anti-oxidative effect of PEG-b-PPS-Rg3 was also evaluated. Oxidative stress plays a remarkable role in the MIRI, and can be reflected by the levels of SOD and MDA [37]. The levels of SOD reduced after I/R, and this decrease was greatly blocked by treatment of PEG-b-PPS-Rg3 (Fig. 5A). The levels of MDA decreased after the intramyocardial injection of PEG-b-PPS-Rg3 compared with the model group (Fig. 5B). HO-1/Nrf2 signal pathway, which was regulated by activation of Sirt1 and PGC-α, is an important cellular defense process against oxidative stress caused by MIRI [38,39]. In the model group, the expression of proteins regulating oxidative stress, including Sirt1, PGC-1α, Nrf1/2, HO-1, and SOD1, was downregulated, but upregulated after the intramyocardial injection of PEG-b-PPS-Rg3 (Fig. 5C, D). The PEG-b-PPS showed no obvious effect in increasing the expression of proteins related to the oxidative stress (Fig. 5C, D). These results indicated that PEG-b-PPS-Rg3 reduced the heart injury caused by the oxidative stress.

3.6. PEG-b-PPS-Rg3 nanoparticles exerted anti-inflammatory effects in rats with MIRI

The anti-inflammatory effects of PEG-b-PPS-Rg3 was further assessed. The expression of TNF-α was obviously increased in the model and PEG-b-PPS group, but was abated after administration of PEG-b-PPS-Rg3 (Fig. 6A). Moreover, the expression of inflammatory factors and their corresponding signal pathways were evaluated. ELISA analysis displayed that after the injection of PEG-b-PPS-Rg3, the expression of IL-6, IL-1β, TNF-α, and CRP in plasma was noticeably decreased compared with that in model and PEG-b-PPS group (Fig. 6B). Phosphorylation of IκBα induced NF-κB translocation from the cytosol to the nucleus and increased the expression of many inflammatory factors [40]. The phosphorylation of NF-κB (transfer from the cytoplasm to the nucleus) was suppressed in the PEG-b-PPS-Rg3 group compared with the model group (Fig. 6C, D). The expression of phosphorylation of IκBα was lower compared to the model group after the injection of PEG-b-PPS-Rg3 (Fig. 6C, D). These results demonstrated that PEG-b-PPS-Rg3 exerted anti-inflammatory effects by inhibiting NF-κB activation.

3.7. PEG-b-PPS-Rg3 nanoparticles exerted anti-fibrotic effects in rats with MIRI

The activation of TGF-β/Smad signaling is considered to be a key event in the progression of tissue fibrosis [41]. Sirius red staining was used to evaluate collagen deposition to verify the anti-fibrotic effects of PEG-PPS-Rg3 in rats with MIRI. As shown in Fig. 7A, compared with model and PEG-b-PPS group, collagen deposition was markedly decreased after the treatment of PEG-b-PPS-Rg3. However, PEG-b-PPS had no inhibitory effect on collagen deposition. Meanwhile, the blocking of TGF-β/Smad signaling effects of PEG-b-PPS-Rg3 was evaluated using Western blots. Activated TGF-β induced the phosphorylation of Smad2 and Smad3 in the model group more effectively than in the healthy heart (Fig. 7B, C). Compared with the model group, the expression of TGF-β, P-Smad2/Smad2, and P-Smad3/Smad3 exhibited a significant decrease in PEG-b-PPS-Rg3 group (Fig. 7B, C). Moreover, the expression of MMP2 and MMP9 were downregulated after treatment with PEG-b-PPS-Rg3. These results confirmed that PEG-b-PPS-Rg3 decreased myocardial fibrosis by inhibiting the TGF-β-Smad signaling pathway.

3.8. PEG-b-PPS-Rg3 nanoparticles exerted anti-apoptosis effects in rats with MIRI

Finally, the anti-apoptotic activity of PEG-b-PPS-Rg3 was determined by TUNEL staining and Western blot analysis. There was a higher number of TUNEL-positive cells in the model group than in the sham group; numbers of TUNEL-stained cells decreased in the PEG-b-PPS-Rg3 treatment group (Fig. 8A). Western blot analysis showed that the expression of Bax (a promoter of apoptosis) was attenuated, and the expression of Bcl-2 (an inhibitor of apoptosis) was increased in the PEG-b-PPS-Rg3 group, compared with the model group (Fig. 8B, C). These results established that PEG-b-PPS-Rg3 exerted an anti-apoptotic effect in rats with MIRI.

4. Discussion

The high incidence and mortality of acute myocardial infarction have long threatened human health and longevity [1,4]. Treatments such as thrombolysis or percutaneous coronary intervention can result in severe MIRI [3,5]. As MIRI is predominantly caused by excessive production of ROS [42], an ROS-responsive drug delivery system would be an appropriate treatment strategy method to release drugs at the injury site and reduce drug accumulation. Furthermore, the elucidation of targets and mechanisms of drug action is necessary for drug development. This study showed that intramyocardial injection of PEG-b-PPS-Rg3 released Rg3 in response to ROS at the injury site. Rg3 then targeted FoxO3a, activated its downstream signaling pathways and led to the inhibition of oxidative stress, inflammation, apoptosis and fibrosis; achieving effective treatment of MIRI.

Rg3 is a hydrophobic compound with various pharmacological activities. However, its poor bioavailability leads to a low therapeutic effect [14,43]. Therefore, the development of an appropriate drug loading and delivery approach for Rg3 to achieve stimuli-responsive release of Rg3 to the local tissue microenvironment can help improve its efficacy. Previous studies used Pluronics FI 27 encapsulated Rg3 to enhance its solubility and antioxidant effects in a doxorubicin-induced heart injury model [14]. Pluronics F127 copolymer is homologous to PEG-b-PPS; differing in an oxygen atom and a sulfur atom in the hydrophobic domain, which results in PEG-b-PPS having more hydrophobicity than Pluronics F127. The release rate of Rg3 from PEG-b-PPS-Rg3 was slower over time with the release rate reaching 18.99% in 37 °C PBS by 72 h. The rate of release reached approximately 80% at the same time point, when encapsulated in Pluronics F127 [14].

Therefore, the stability of PEG-b-PPS-loaded hydrophobic drug vesicles was an improvement over those loaded into Pluronics F127. In addition, the release rate of Rg3 in H_2O_2 (1 mM) was significantly higher than that in PBS (80.44% vs. 18.99%), indicating that the stability of PEG-b-PPS-Rg3 in H_2O_2 was much lower than that of PBS; thus generating a successful ROS-responsive release system. Furthermore, PEG-b-PPS-Rg3 released Rg3 at ROS-generating sites and was subsequently transformed into hydrophilic fragments, allowing for its removal and elimination. These results indicated that PEG-b-PPS-Rg3 had potential for use in clinical applications for treating diseases related to oxidative damage.

In the design and development of new drugs, identification of therapeutic targets is an imperative step. Exploring the pharmacophore model and the quantitative structure-activity relationship between a drug of known biological activity and its target is important in the optimization of drug structure; to enhance activity and reduce its toxic side effects. The target and mechanism of action of Rg3 have yet to be clarified, a fact that hinders the development of Rg3 as an effective drug for the treatment of cardiovascular diseases. In the present study, molecular docking was used to screen putative protein molecule interactions with Rg3. The results showed that Rg3 and FoxO3a had a tight conformational coupling; the maximum binding affinity between Rg3 and FoxO3a was −6.0 kcal/mol. The binding affinity of most natural products targeting proteins is estimated to be approximately −2.0 kcal/mol [44–46], suggesting that Rg3 would have highly specific targeting and a better development potential, compared to other natural protein products. FoxQ3a is a key protein involved in regulating antioxidant reactions. Activated FoxO3a reduces oxidative stress injury in I/R models by enhancing SOD activity [47,48]. In rat I/R models, FoxO3a enhanced mitochondrial autophagy by activating the Sirt-1 pathway, resulting in lower ROS production [49]. In this study, FoxO3a shRNA adenovirus was used to knockdown *FoxO3a* in H9C2 cells, to verify that FoxO3a was a key target for Rg3. Rg3 had no effect on viability and apoptosis when FoxO3a was knocked-down in H/R-injured H9C2 cells. Furthermore, Rg3 did not protect mitochondrial homeostasis or show an anti-oxidative stress effect when FoxO3a was knocked-down. The process of organ fibrosis is classically promoted by activation of the TGF-β/Smad signaling pathway [41,50], which has been shown to be regulated by FoxO3a [51]. In addition, FoxO3a inhibited the release of inflammatory factors by regulating the NF-KP/ IKK-induced inflammatory cascades [52]. Here, we showed that in rat models of MIRI, Rg3 regulated FoxO3a and inhibited its downstream signaling pathways, including those for oxidative stress, inflammation, fibrosis and apoptosis. Therefore, FoxO3a was confirmed to be a key target of Rg3 in the treatment of MIRI. This discovery might facilitate the development of Rg3 as a therapeutic drug for cardiovascular diseases and serve as reference for the screening of targets and exploring mechanisms of action for natural products.

A new treatment strategy of catheter-based endocardial or intramyocardial injections has shown improvements in therapeutic effects compared with traditional treatments, including intravenous and abdominal injections. This strategy has been applied in clinical trials for the treatment of cardiovascular diseases [53–55]. In the present study, I/R rat models received intramyocardial injection of PEG-b-PPS-Rg3, which reduced mortality compared with that for the injection of free Rg3 (10% vs 60%, $n = 10$, Fig. S1B) and exhibited excellent histocompatibility. We showed that the accumulation of free Rg3, due to its low solubility, led to cardiac microvascular obstruction. This result suggested that PEG-b-PPS-Rg3 could be effectively used in the clinic for catheter-based myocardial *in situ* injections. In future studies, FoxO3a conditional knockdown rats should be used to demonstrate the effect of Rg3 on the regulation of FoxO3a, especially in treating MIRI. Moreover, designing drug-loaded nanoparticles with targeting modifications may help achieve non-invasive systematic delivery for tissue-specific drug release.

In conclusion, Rg3-loaded PEG-b-PPS nanoparticles responded to ROS, and the released Rg3 alleviated MIRI by interacting with the target protein, FoxO3a; inhibited its downstream signaling pathways, including those for oxidative stress, inflammation and fibrosis. This study also identified the therapeutic target and mechanism of action of Rg3 in treating MIRI. In addition, we showed the effective treatment of local damage to the tissue microenvironment through the use of ROS-responsive polymer vesicles. These results serve as a platform to help accelerate the development of Rg3 as a clinical treatment for cardiovascular diseases, as well as providing a reference for the exploration of therapeutic targets and the optimization of formulations for other natural drug products (Fig. 9).

Supplementary Material

Refer to Web version on PubMed Central for supplementary material.

Acknowledgment

This work was supported by grants from the National Key Subject of Drug Innovation (2018ZX09201009-007), National Key R&D Program of China (NO. 2018YFC1704500 and 2017YFC1103500), National Natural Science Foundation of China project (81774050, 81972063, 31700845, 81904054), and the Tianjin Science Foundation for Distinguished Young Scholars (17JCJQJC46200), Training Program Foundation for Innovative Research Team of Higher Education in Tianjin during the 13th Five-Year Plan Period (NO.TD13-5050), National Science Foundation, United States (NSF-DMR award number 1508511), NIAMS, United States award number 1R01AR067859, and the CSC Scholarships.

References

[1]. Reed GW, Rossi JE, Cannon CP, Acute myocardial infarction, Lancet 389 (2017) 197–210. [PubMed: 27502078]

[2]. Magro M, Garg S, Serruys PW, Revascularization treatment of stable coronary artery disease, Expert. Opin. Pharmacother. 12 (2011) 195–212. [PubMed: 21226632]

[3]. Wu J, Hall M, Dondo TB, Wilkinson C, Ludman P, DeBelder M, Fox KAA, Timmis A, Gale CP Association between time of hospitalization with acute myocardial infarction and in-hospital mortality, Eur. Heart J. 40 (2019) 1214–1221. [PubMed: 30698766]

[4]. Frohlich GM, Meier P, White SK, Yellon DM, Hausenloy DJ, Myocardial reperfusion injury: looking beyond primary PCI, Eur. Heart J. 34 (2013) 1714–1722. [PubMed: 23536610]

[5]. Murphy E, Steenbergen C, Mechanisms underlying acute protection from cardiac ischemia-reperfusion injury, Physiol. Rev. 88 (2008) 581–609. [PubMed: 18391174]

[6]. Chouchani ET, Pell VR, Gaude E, Aksentijevic D, Sundier SY, Robb EL, Logan A, Nadtochiy SM, Ord ENJ, Smith AC, Eyassu F, Shirley R, Hu CH, Dare AJ, James AM, Rogatti S, Hartley RC, Eaton S, Costa ASH, Brookes PS, Davidson SM, Duchen MR, Saeb-Parsy K, Shattock MJ, Robinson AJ, Work LM, Frezza C, Krieg T, Murphy MP, Ischaemic accumulation of succinate controls reperfusion injury through mitochondrial ROS, Nature 515 (2014) 431–435. [PubMed: 25383517]

[7]. Feng S, Hu Y, Peng S, Han S, Tao H, Zhang Q, Xu X, Zhang J, Hu H, Nanoparticles responsive to the inflammatory microenvironment for targeted treatment of arterial restenosis, Biomaterials 105 (2016) 167–184. [PubMed: 27522252]

[8]. Lee D, Bae S, Hong D, Lim H, Yoon JH, Hwang O, Park S, Ke Q, Khang G, Kang PM, H202-responsive molecularly engineered polymer nanoparticles as ischemia/reperfusion-targeted nanotherapeutic agents, Sci. Rep. 3 (2013) 2233. [PubMed: 23868607]

[9]. Hao P, Jiang F, Cheng J, Ma L, Zhang Y, Zhao Y, Traditional Chinese medicine for cardiovascular disease: evidence and potential mechanisms, J. Am. Coll. Cardiol. 69 (2017) 2952–2966. [PubMed: 28619197]

[10]. Smith I, Williamson EM, Putnam S, Farrimond J, Whalley BJ, Effects and mechanisms of ginseng and ginsenosides on cognition, Nutr. Rev. 72 (2014) 319–333. [PubMed: 24666107]

[11]. Kim SJ, Jang JY, Kim EJ, Cho EK, Ahn DG, Kim C, Park HS, Jeong SW, Lee SH, Kim SG, Kim YS, Kim HS, Kim BS, Lee J, Siddiqui A, Ginsenoside Rg3 restores hepatitis C virus-induced aberrant mitochondrial dynamics and inhibits virus propagation, Hepatology 66 (2017) 758–771.. [PubMed: 28329914]

[12]. Cheng L, Sun X, Zhao X, Wang L, Yu J, Pan G, Li B, Yang H, Zhang Y, Cui W, Surface biofunctional drug-loaded electrospun fibrous scaffolds for comprehensive repairing hypertrophic scars, Biomaterials 83 (2016) 169–181. [PubMed: 26774564]

[13]. Cheng L, Sun X, Hu C, Jin R, Sun B, Shi Y, Zhang L, Cui W, Zhang Y, In vivo inhibition of hypertrophic scars by implantable ginsenoside-Rg3-loaded electrospun fibrous membranes, Acta Biomater. 9 (2013) 9461–9473. [PubMed: 23938200]

[14]. Li L, Ni J, Li M, Chen J, Han L, Zhu Y, Kong D, Mao J, Wang Y, Zhang B, Zhu M, Gao X, Fan G, Ginsenoside Rg3 micelles mitigate doxorubicin-induced cardiotoxicity and enhance its anticancer efficacy, Drug Deliv. 24 (2017) 1617–1630. [PubMed: 29063791]

[15]. Zhang LP, Jiang YC, Yu XF, Xu HL, Li M, Zhao XZ, Sui DY, Ginsenoside Rg3 improves cardiac function after myocardial ischemia/reperfusion via attenuating apoptosis and inflammation, Evid. Based Complement. Alternat. Med. 2016 (2016) 6967853. [PubMed: 28105061]

[16]. Wang Y, Hu Z, Sun B, Xu J, Jiang J, Luo M, Ginsenoside Rg3 attenuates myocardial ischemia/reperfusion injury via Akt/endothelial nitric oxide synthase signaling and the Bcell lymphoma/Bcell lymphoma associated X protein pathway, Mol. Med. Rep. 11 (2015) 4518–4524. [PubMed: 25672441]

[17]. Rosier A, Vandermeulen GW, A Klok H, Advanced drug delivery devices via self-assembly of amphiphilic block copolymers, Adv. Drug Deliv. Rev. 53 (2001) 95–108. [PubMed: 11733119]

[18]. Gu L, Faig A, Abdelhamid D, Uhrich K, Sugar-based amphiphilic polymers for biomedical applications: from nanocarriers to therapeutics, Acc. Chem. Res. 47 (2014) 2867–2877. [PubMed: 25141069]

[19]. Napoli A, Valentini M, Tirelli N, Muller M, Hub bell JA, Oxidation-responsive polymeric vesicles, Nat. Mater. 3 (2004) 183–189. [PubMed: 14991021]

[20]. Cerritelli S, O'Neil CP, Velluto D, Fontana A, Adrian M, Dubochet J, Hubbell JA, Aggregation behavior of poly(ethylene glycol-bl-propylene sulfide) di- and triblock copolymers in aqueous solution, Langmuir 25 (2009) 11328–11335. [PubMed: 19711914]

[21]. Velluto D, Demurtas D, Hubbell JA, PEG-b-PPS diblock copolymer aggregates for hydrophobic drug solubilization and release: cyclosporin a as an example, Mol. Pharm. 5 (2008) 632–642. [PubMed: 18547055]

[22]. Chen G, You G, Wang Y, Lu M, Cheng W, Yang J, Zhao L, Zhou H, Effects of synthetic colloids on oxidative stress and inflammatory response in hemorrhagic shock: comparison of hydroxyethyl starch 130/0.4, hydroxyethyl starch 200/0.5, and succinylated gelatin, Crit. Care 17 (2013) R141. [PubMed: 23849347]

[23]. Chen G, Deng H, Song X, Lu M, Zhao L, Xia S, You G, Zhao J, Zhang Y, Dong A, Zhou H, Reactive oxygen species-responsive polymeric nanoparticles for alleviating sepsis-induced acute liver injury in mice, Biomaterials 144 (2017) 30–41. [PubMed: 28820966]

[24]. de Couto G, Gallet R, Cambier L, Jaghatspanyan E, Makkar N, Dawkins JF, Berman BP, Marban E, Exosomal MicroRNA transfer into macrophages mediates cellular Postconditioning, Circulation 136 (2017) 200–214. [PubMed: 28411247]

[25]. Yang X, Li H, Qian C, Guo Y, Li C, Gao F, Yang Y, Wang K, Oupicky D, Sun M, Near-infrared light-activated IR780-loaded liposomes for anti-tumor angiogenesis and Photo thermal therapy, Nanomedicine 14 (2018) 2283–2294. [PubMed: 29981460]

[26]. Zhou Z, Li C, Zhang M, Zhang Q, Qian C, Oupicky D, Sun M, Charge and assembly reversible micelles Fueled by intracellular ATP for improved siRNA transfection, ACS Appl. Mater. Interfaces 10 (2018) 32026–32037. [PubMed: 30179452]

[27]. Zhou Z, Liu Y, Zhang M, Li C, Yang R, Li J, Qian C, Sun M, Size switchable nanoclusters Fueled by extracellular ATP for promoting deep penetration and MRI-guided tumor Photo thermal therapy, Adv. Funct. Mater. 29 (2019) 1904144.

[28]. Fan G, Yu J, Asare PF, Wang L, Zhang H, Zhang B, Zhu Y, Gao X, Danshensu alleviates cardiac ischaemia/reperfusion injury by inhibiting autophagy and apoptosis via activation of mTOR signalling, J. Cell. Mol. Med. 20 (2016) 1908–1919. [PubMed: 27385290]

[29]. Yang X, Yang Y, Gao F, Wei JJ, Qian CG, Sun MJ, Biomimetic hybrid Nanozymes with self-supplied H(+) and accelerated 02 generation for enhanced starvation and photodynamic therapy against hypoxic Tumors, Nano Lett. 19 (2019) 4334–4342. [PubMed: 31179709]

[30]. Livingston MJ, Wang J, Zhou J, Wu G, Ganley IG, Hill JA, Yin XM, Dong Z, Clearance of damaged mitochondria via mitophagy is important to the protective effect of ischemic preconditioning in kidneys, Autophagy (2019) 1–21.

[31]. Trott O, Olson AJ, AutoDock Vina: improving the speed and accuracy of docking with a new scoring function, efficient optimization, and multithreading, J. Comput. Chem. 31 (2010) 455–461. [PubMed: 19499576]

[32]. Sanner MF, Python: a programming language for software integration and development, J. Mol. Graph Model 17 (1999) 57–61. [PubMed: 10660911]

[33]. Morris GM, Huey R, Lindstrom W, Sanner MF, Belew RK, Goodsell DS, Olson AJ, AutoDock4 and AutoDockTools4: automated docking with selective receptor flexibility, J. Comput. Chem. 30 (2009) 2785–2791. [PubMed: 19399780]

[34]. Santiago AP, Chaves EA, Oliveira MF, Galina A, Reactive oxygen species generation is modulated by mitochondrial kinases: correlation with mitochondrial antioxidant peroxidases in rat tissues, Biochimie 90 (2008) 1566–1577. [PubMed: 18634844]

[35]. Wu QF, Qian C, Zhao N, Dong Q, Li J, Wang BB, Chen L, Yu L, Han B, Du YM, Liao YH, Activation of transient receptor potential vanilloid 4 involves in hypoxia/reoxygenation injury in cardiomyocytes, Cell Death Dis. 8 (2017) e2828. [PubMed: 28542130]

[36]. Chen JR, Wei J, Wang LY, Zhu Y, Li L, Olunga MA, Gao XM, Fan GW, Cardioprotection against ischemia/reperfusion injury by QiShenYiQi pill(R) via ameliorate of multiple mitochondrial dysfunctions, Drug Des. Devel. Ther. 9 (2015) 3051–3066.

[37]. Li H, Horke S, Forstermann U, Oxidative stress in vascular disease and its pharmacological prevention, Trends Pharmacol. Sci. 34 (2013) 313–319. [PubMed: 23608227]

[38]. Do MT, Kim HG, Choi JH, Jeong HG, Metformin induces microRNA-34a to downregulate the Sirtl/Pgc-la/Nrf2 pathway, leading to increased susceptibility of wild-type p53 cancer cells to oxidative stress and therapeutic agents, Free Radic. Biol. Med. 74 (2014) 21–34. [PubMed: 24970682]

[39]. Marie L, Carmen A, Zachary GH, Hamid M, Carles L, Frederic D, Nadia M, Jill M, Philip L, Peter E, Resveratrol improves mitochondrial function and protects against metabolic disease by activating SIRT1 and PGC-lalpha, Cell 127 (2006) 1109–1122. [PubMed: 17112576]

[40]. Takada Y, Mukhopadhyay A, Kundu GC, Mahabeleshwar GH, Singh S, Aggarwal BB, Hydrogen peroxide activates NF-κB through tyrosine phosphorylation of Iκ2α and serine phosphorylation of p65 evidence for the involvement OF Iκ2α kinase AND Syk PROTEIN-TYROSINE KINASE, J. Biol. Chem. 278 (2003) 24233–24241. [PubMed: 12711606]

[41]. Park SA, Kim MJ, Park SY, Kim JS, Lee SJ, Woo HA, Kim DK, Nam JS, Sheen YY, EW-7197 inhibits hepatic, renal, and pulmonary fibrosis by blocking TGF-beta/Smad and ROS signaling, Cell. Mol. Life Sci. 72 (2015) 2023–2039. [PubMed: 25487606]

[42]. Collet C, Capodanno D, Onuma Y, Banning A, Stone GW, Taggart DP, Sabik J, Serruys PW, Left main coronary artery disease: pathophysiology, diagnosis, and treatment, Nat. Rev. Cardiol. 15 (2018) 321–331. [PubMed: 29599504]

[43]. Yang LQ, Wang B, Gan H, Fu ST, Zhu XX, Wu ZN, Zhan DW, Gu RL, Dou GF, Meng ZY, Enhanced oral bioavailability and anti-tumour effect of paclitaxel by 20(s)-ginsenoside Rg3 in vivo, Biopharm. Drug Dispos. 33 (2012) 425–436. [PubMed: 22898996]

[44]. Wei J, Chen JR, Pais EMA, Wang TY, Miao L, Li L, Li LY, Qiu F, Hu LM, Gao XM, Fan GW, Oxyresveratrol is a phytoestrogen exerting anti-inflammatory effects through NF-kappaB and estrogen receptor signaling, Inflammation 40 (2017) 1285–1296. [PubMed: 28484893]

[45]. Yin S, Qiu Y, Jin C, Wang R, Wu S, Liu H, Koo S, Han L, Zhang Y, Gao X, Pang X, Wang T, Yu H, 7-Deoxynarciclasine shows promising antitumor efficacy by targeting Akt against hepatocellular carcinoma, Int. J. Cancer 145 (2019) 3334–3346. [PubMed: 31081930]

[46]. Scotti L, Bezerra Mendonca FJ, Ribeiro FF, Tavares JF, da Silva MS, Barbosa Filho JM, Scotti MT, Natural product inhibitors of topoisomerases: review and docking study, Curr. Protein Pept. Sci. 19 (2018) 275–291.

[47]. Kim J, Toda T, Watanabe K, Shibuya S, Ozawa Y, Izuo N, Cho S, Seo DB, Yokote K, Shimizu T, Syringaresinol reverses age-related skin atrophy by suppressing FoxO3a-mediated matrix Metalloproteinase-2 activation in copper/zinc superoxide dismutase-deficient mice, J. Invest. Dermatol. 139 (2019) 648–655. [PubMed: 30798853]

[48]. Chang G, Chen Y, Zhang H, Zhou W, Trans sodium crocetinate alleviates ischemia/reperfusion-induced myocardial oxidative stress and apoptosis via the SIRT3/F0X03a/S0D2 signaling pathway, Int. Immunopharmacol. 71 (2019) 361–371. [PubMed: 30952100]

[49]. Dusabimana T, Kim SR, Kim HJ, Park SW, Kim H, Nobiletin ameliorates hepatic ischemia and reperfusion injury through the activation of SIRT-l/F0X03a-mediated autophagy and mitochondrial biogenesis, Exp. Mol. Med. 51 (2019) 51.

[50]. Yu M, Zhao M, Yu R, Chu S, Xu J, Xia M, Wang C, Nanotechnology-mediated immunochemotherapy with Ingenol-3-Mebutate for systematic anti-tumor effects, J. Control. Release 304 (2019) 242–258. [PubMed: 31071376]

[51]. Kato M, Yuan H, Xu ZG, Lanting L, Li SL, Wang M, Hu MC, Reddy MA, Natarajan R, Role of the Akt/FoxO3a pathway in TGF-betal-mediated mesangial cell dysfunction: a novel mechanism related to diabetic kidney disease, J. Am. Soc. Nephrol. 17 (2006) 3325–3335. [PubMed: 17082237]

[52]. Bale S, Pulivendala G, Godugu C, Withaferin a attenuates bleomycin-induced scleroderma by targeting FoxO3a and NF-kappabeta signaling: connecting fibrosis and inflammation, Biofactors 44 (2018) 507–517. [PubMed: 30367690]

[53]. Patel AN, Henry TD, Quyyumi AA, Schaer GL, Anderson RD, Toma C, East C, Remmers AE, Goodrich J, Desai AS, Recker D, DeMaria A, Ixmyelocel-T for patients with ischaemic heart failure: a prospective randomised double-blind trial, Lancet 387 (2016) 2412–2421. [PubMed: 27059887]

[54]. Yau TM, Pagani FD, Mancini DM, Chang HL, Lala A, Woo YJ, Acker MA, Selzman CH, Soltesz EG, Kern JA, Maltais S, Charbonneau E, Pan S, Marks ME, Moquete EG, O'Sullivan KL, Taddei-Peters WC, McGowan LK, Green C, Rose EA, Jeffries N, Parides MK, Weisel RD, Miller MA, Hung J, O'Gara PT, Moskowitz AJ, Gelijns AC, Bagiella E, Milano CA, Intramyocardial injection of mesenchymal precursor cells and successful temporary weaning from left ventricular assist device support in patients with advanced heart failure: a randomized clinical trial, Jama 321 (2019) 1176–1186. [PubMed: 30912838]

[55]. van Ramshorst J, Bax JJ, Beeres SL, Dibbets-Schneider P, Roes SD, Stokkel MP, de Roos A, Fibbe WE, Zwaginga JJ, Boersma E, Schalij MJ, Atsma DE, Intramyocardial bone marrow cell injection for chronic myocardial ischemia: a randomized controlled trial, Jama 301 (2009) 1997–2004. [PubMed: 19454638]

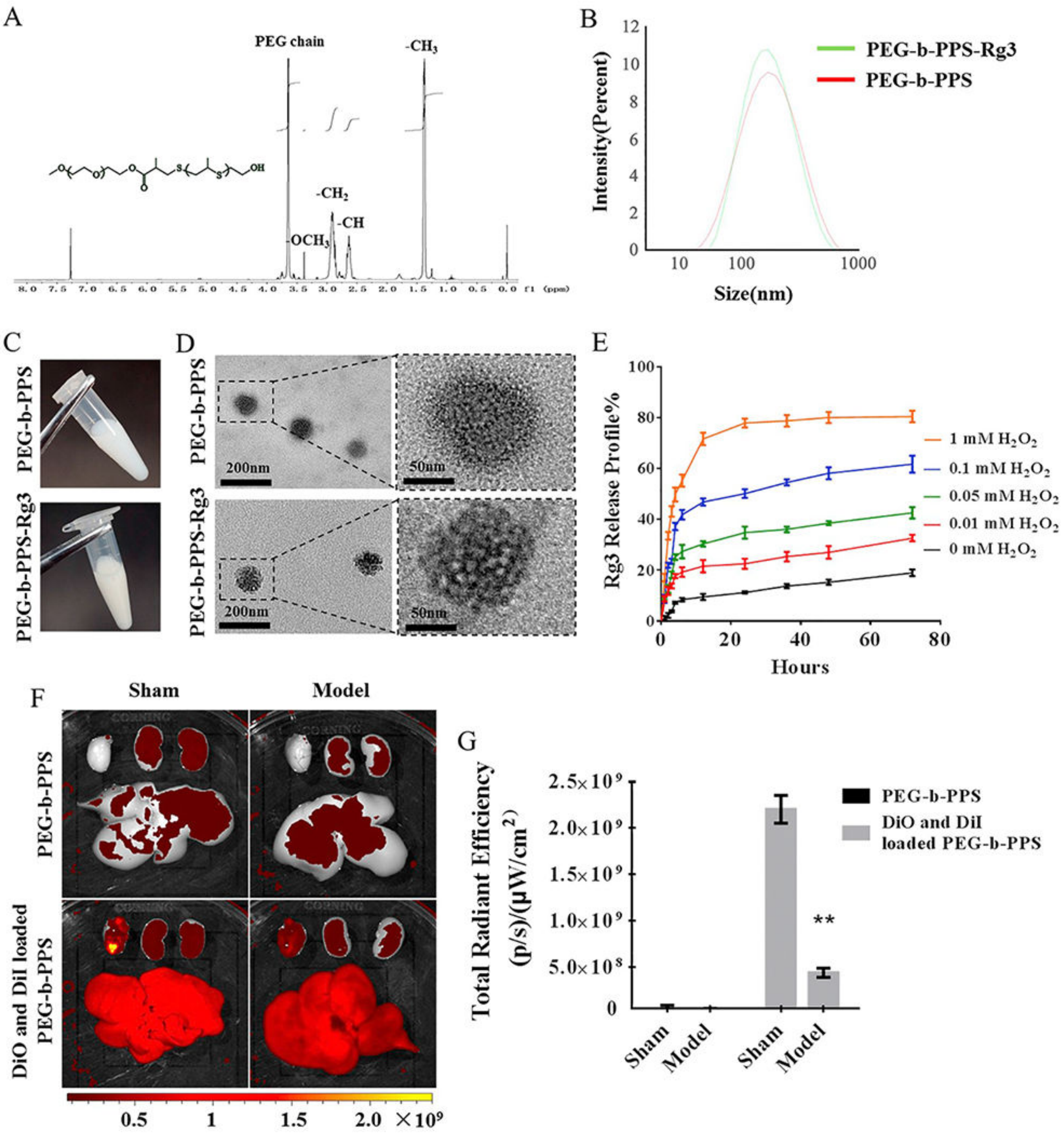

Fig. 1.

Characterization and release profile of PEG-b-PPS-Rg3 nanoparticles. (A) ^{1}H NMR spectrum of PEG-b-PPS. ^{1}H NMR ($CDC1_3$): δ = 1.30–1.40 ppm (−CH_3 in PPS chain), 2.6–2.7 ppm (-CH in PPS chain), 2.80–3.0 ppm (−CH_2 in PPS chain), 3.25–3.35 ppm (−OCH_3), 3.5–3.75 ppm (PEG chain protons). (B) Size distribution of PEG-b-PPS and PEG-b-PPS-Rg3 as determined by DLS. (C) Appearance of PEG-b-PPS and PEG-b-PPS-Rg3. (D) TEM image showing the morphology of PEG-b-PPS and PEG-b-PPS-Rg3. (left: scale bar = 200 nm; right: scale bar = 50 nm). (E) Release profiles of PEG-b-PPS-Rg3 in the presence of 0, 0.01, 0.05, 0.1, and 1 mM H_2O_2 (n = 3 per group). (F) Representative FRET images of DiO and DiI co-loaded PEG-b-PPS release in rat hearts. (G) Total radiant efficiency according to FRET in the sham and model groups (n = 3 per group). Data are presented as means ± SD, $^{**}p < .01$ compared with the sham group.

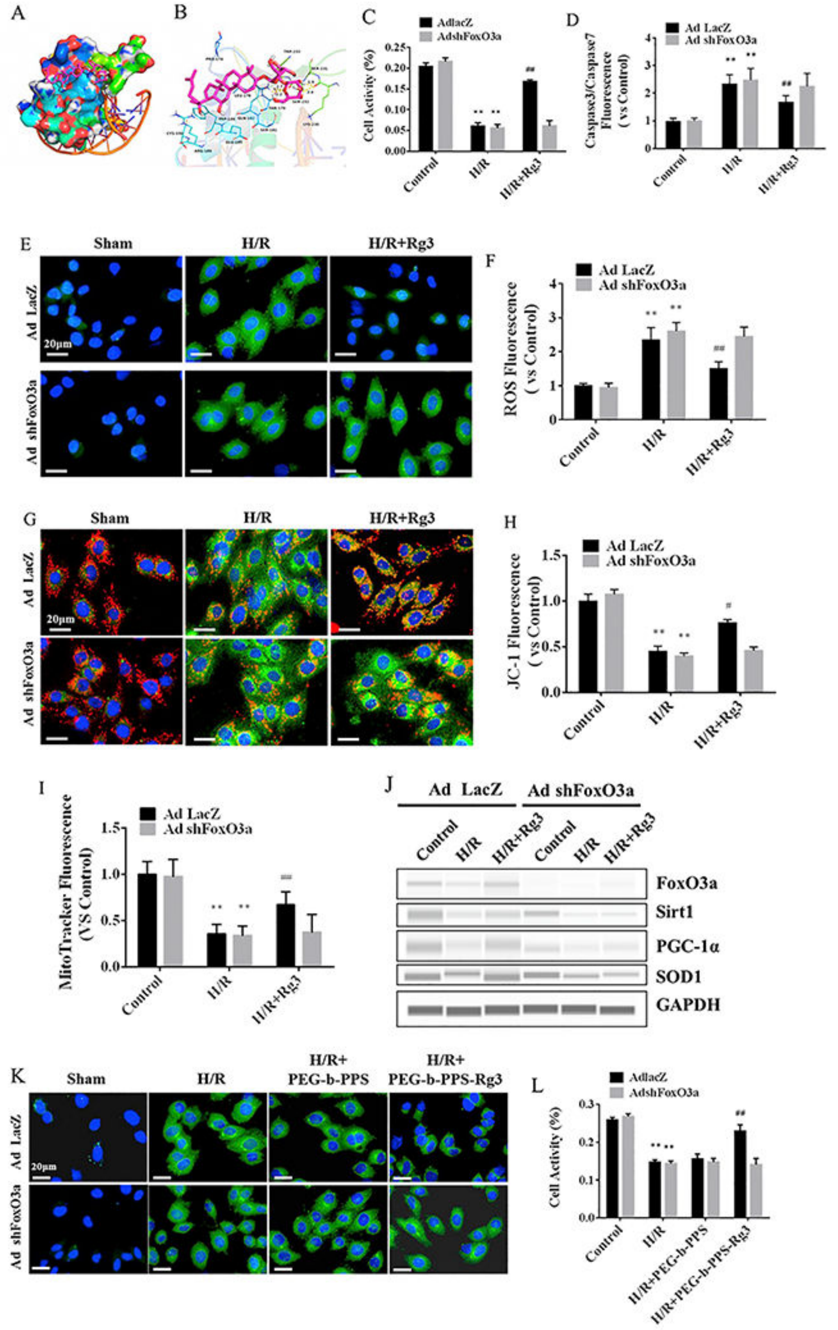

Fig. 2.

Rg3 exerts anti-oxidative activity by binding to FoxO3a. (A) Molecular docking showing Rg3 in the binding site of FoxO3a (total view). (B) Detailed view of the binding between the Rg3 and FoxO3a. FoxO3a is represented by a cartoon, and the representative binding residues are shown as lines; Rg3 is represented with red lines; hydrogen bonds are shown as yellow dotted lines. (C) Activity of H9C2 cells, measured by MTT, with or without knockdown of FoxO3a after administration Rg3 (*n* = 3 per group). (D) Cell apoptosis was measured by a caspase3/7 fluorescent probe with or without knockdown of FoxO3a. (E)

Representative ROS staining (DCFH-DA fluorescent probe) with or without knockdown of FoxO3a after administration Rg3 (scale bar = 20 μm). (F) The levels of ROS in H9C2 cells were determined by a DCFH-DA fluorescent probe with or without knockdown of FoxO3a ($n = 3$ per group). (G) Mitochondrial membrane potential (ΔΨm) staining (JC-1 fluorescent probe) with or without knockdown of FoxO3a (scale bar = 20 μm). (H) Quantification of fluorescence density of JC-1 (red fluorescence/green fluorescence, n = 3 per group). (I) ΔΨm was measured with a MitoTracker fluorescent probe with or without knockdown of FoxO3a (n = 3 per group). (J) Representative digital western blots for FoxO3a, Sirtl, PGC-1α, SOD1, and GAPDH with or without knockdown of FoxO3a. (K) Representative ROS staining (DCFH-DA fluorescent probe) with or without knockdown of FoxO3a after administration PEG-b-PPS-Rg3 (scale bar = 20 μm). (L) Activity of H9C2 cells, measured by MTT, with or without knockdown of FoxO3a after administration PEG-b-PPS-Rg3 (n = 3 per group). Data are presented as means ± SD from three independent experiments, $^{**}p < .01$ compared with the control group; $^{\#}p < .05$, $^{\#\#}p < .01$ compared with the H/R group. (For interpretation of the references to color in this figure legend, the reader is referred to the web version of this article.)

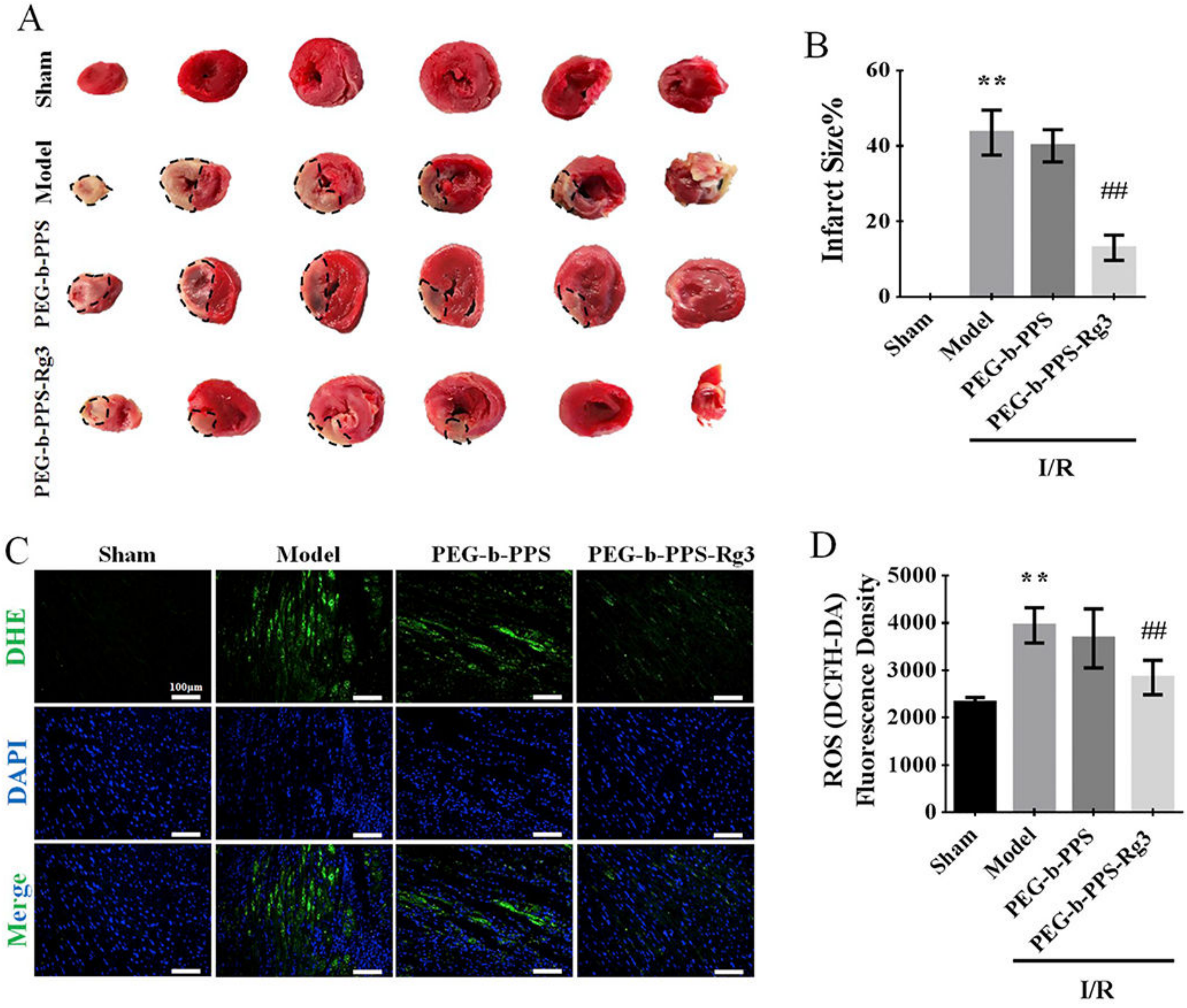

Fig. 3.

PEG-b-PPS-Rg3 in response to ROS and attenuation of myocardial infarction. (A) Representative TTC-stained heart images after 30 min of ischemia and a subsequent 2 h reperfusion treatment. (B) Quantification of infarct sizes in A Percentage Infarct size = (Infarct size /Viable size) x 100%, ($n = 3$ per group). (C) Representative DHE staining of transverse sections of hearts (scale bar = 50 μm). (D) Quantification of fluorescence density in C (n = 3 per group). Data are presented as means ± SD, $^{**}p < .01$ compared with the sham group; $^{\#\#}p < .01$ compared with the model group.

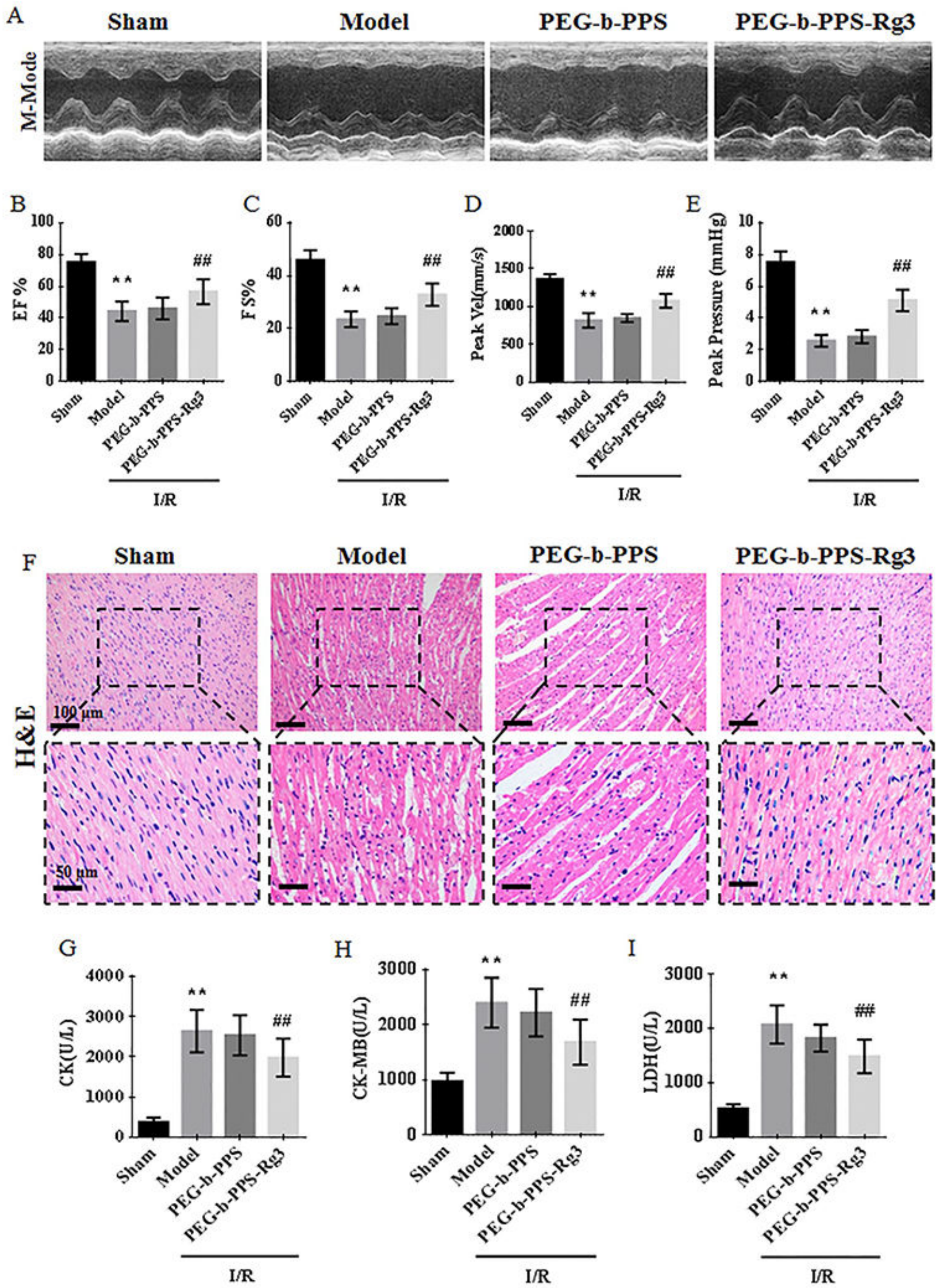

Fig. 4.

PEG-b-PPS-Rg3 nanoparticles improve cardiac functions against MIRI. (A) Representative M-mode echocardiograms for each group. (B-E) Quantification of EF %, FS%, Peak Vel, and peak pressure ($n = 6$ per group). (F) Representative H&E staining of heart transverse sections (scale bar = top, 100 pm; bottom, 50 pm). (G-I) Levels of CK, CK-MB, and LDH in rat serum (n = 6 per group). Data are presented as means ± SD, $^{**}p < .01$ compared with the sham group; $^{\#\#}p < .01$ compared with the model group.

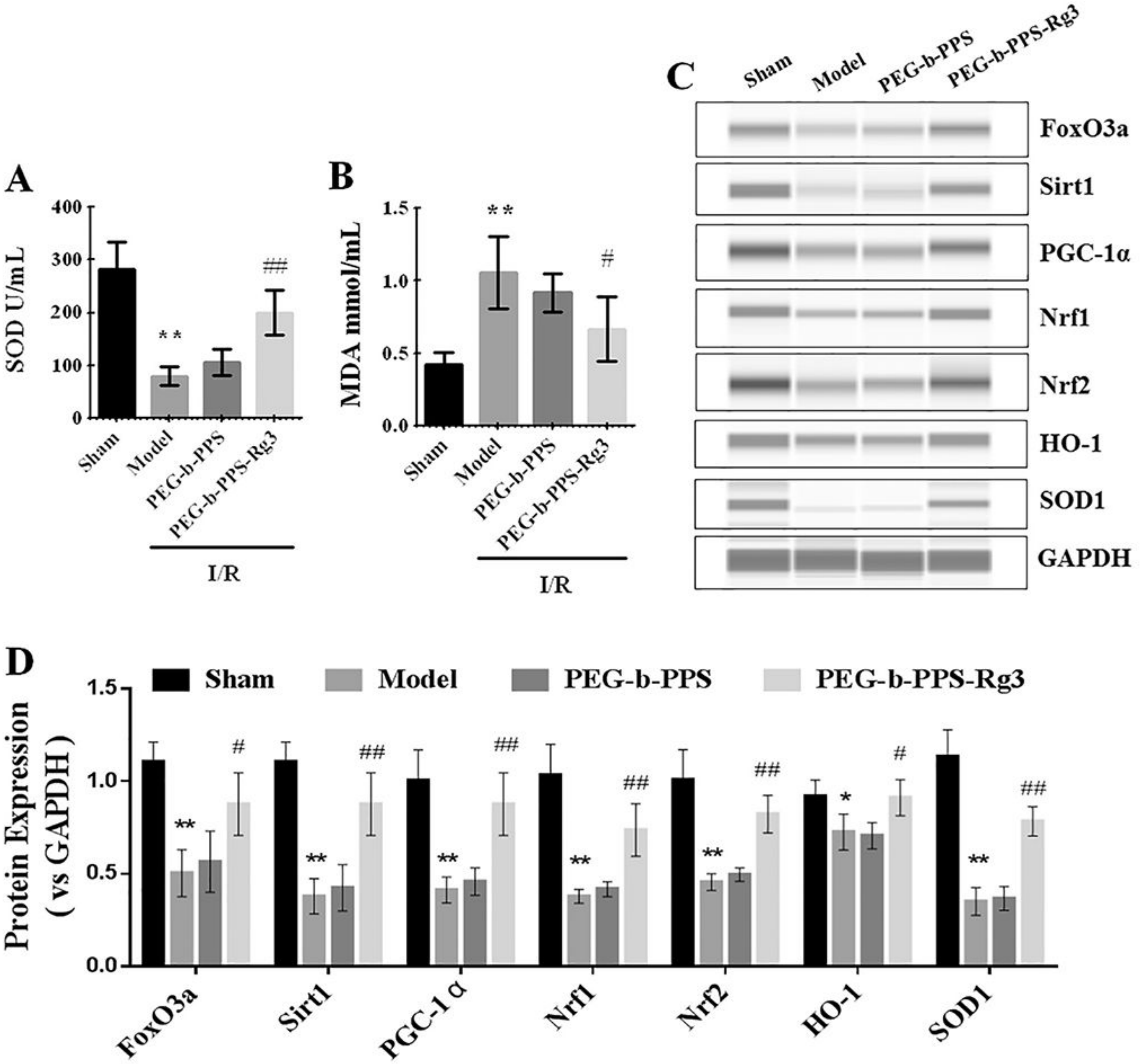

Fig. 5.

PEG-b-PPS-Rg3 exerts anti-oxidative activity in rats. (A, B) The serum levels of SOD and MDA in rats *(n* 6 per group). (C, D) Representative digital western blots of FoxO3a, Sirtl, PGC-1α, Nrf1, Nrf2, HO-1, SOD1 and GAPDH, and corresponding quantitative data (*n* = 3 per group). Data are presented as means ± SD, **p < .01 compared with the sham group; **p* < .05, **p < .01 compared with the model group.

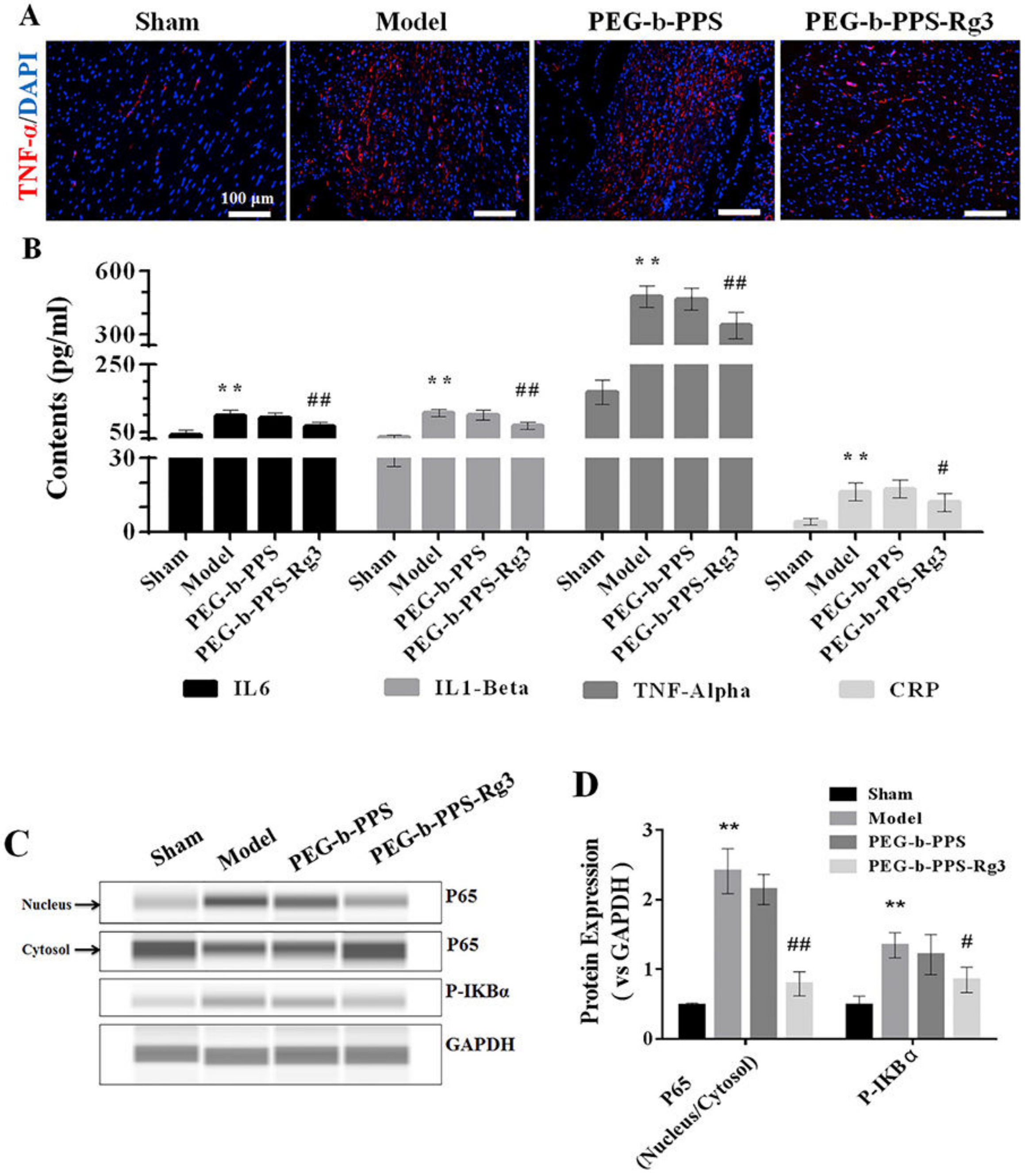

Fig. 6.

PEG-b-PPS-Rg3 exerts anti-inflammatory activity in rats. (A) Representative IF staining of TNF-α (scale bar = 100 μm). (B) The levels of IL6, IL1-β, TNF-α, and CRP in rat serum (n = 6 per group). (C, D) Representative digital western blots for P65 (nucleus), P65 (cytosol), P-IKBα, and GAPDH, and corresponding quantitative data ($n = 3$ per group). Data are presented as means ± SD, $^{**}p < .01$ compared with the sham group; $^{\#}p < .05$, $^{\#\#}p < .01$ compared with the model group.

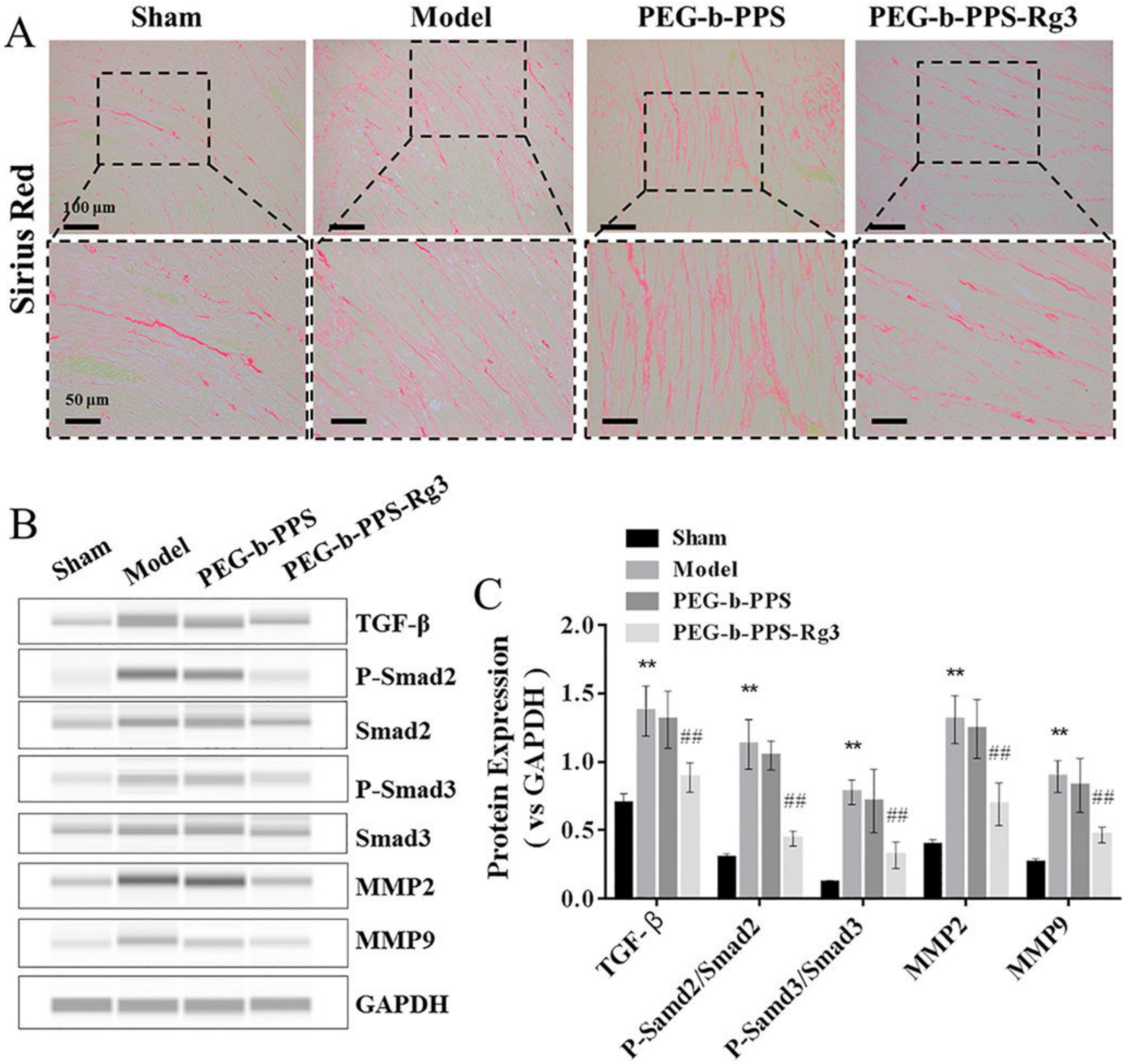

Fig. 7.

PEG-b-PPS-Rg3 exerts anti-fibrotic activity in rats. (A) Collagen deposition was measured by SR staining (scale bar = top, 100 µm; bottom, 50 µm). (B, C) Representative digital western blots of TGF-β, Smad2, P-Smad2, Smad3, P-Smad3, MMP2, MMP9, and GAPDH, and corresponding quantitative data (n = 3 per group). Data are presented as means ± SD from three independent experiments, $^{*}p < .01$ compared with the sham group; $^{\#}p < .05$, $^{\#\#}p < .01$ compared with the model group.

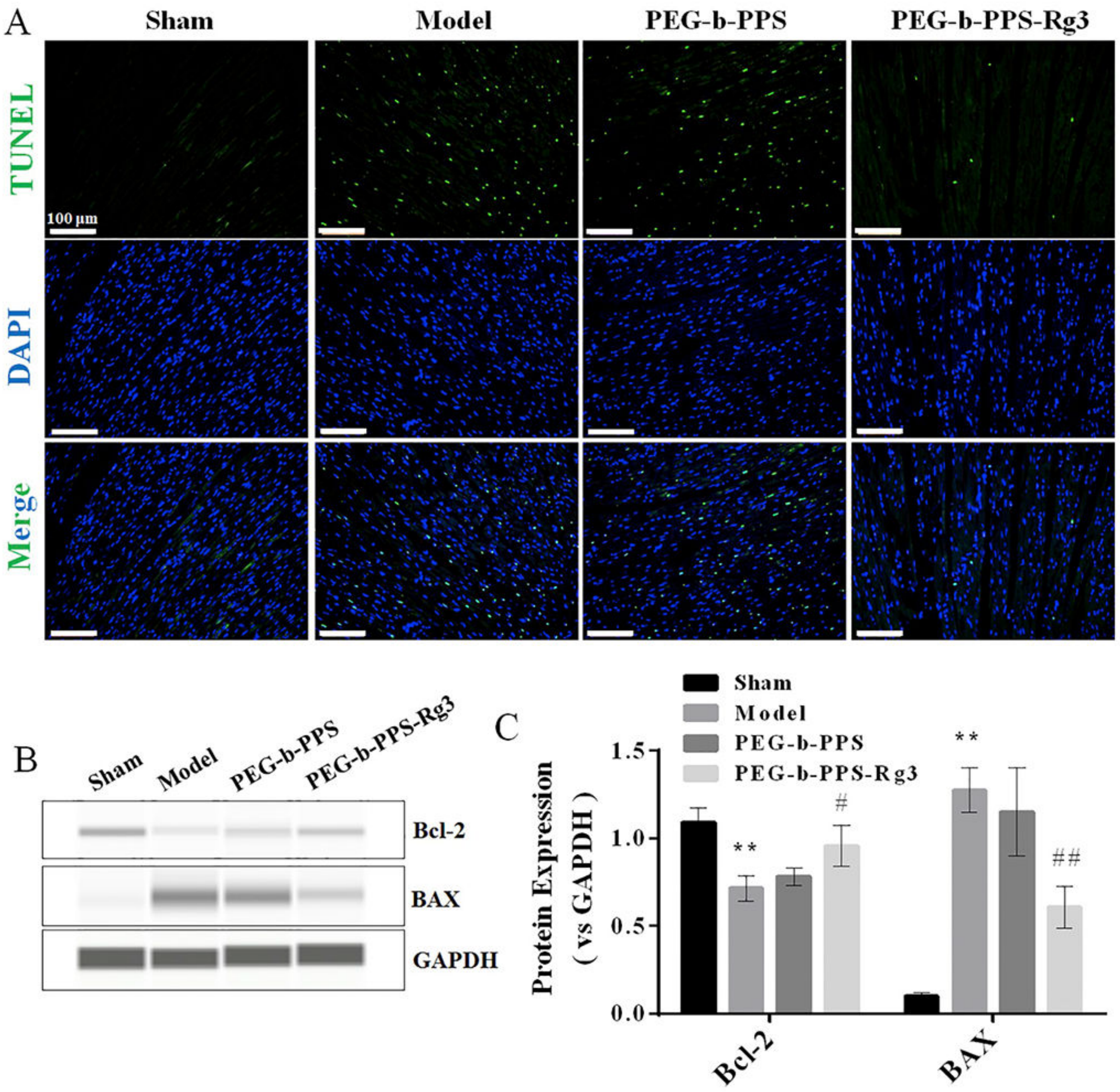

Fig. 8.

PEG-b-PPS-Rg3 exerts anti-apoptotic activity in rats. (A) Representative TUNEL staining of heart transverse sections (scale bar = 100 pm). Apoptotic nuclei were visualized by green fluorescence. Nuclei stained with DAPI are blue. (B, C) Representative digital western blots of BAX, Bcl-2, and GAPDH, and corresponding quantitative data (n = 3 per group). Data are presented as means ± SD from three independent experiments, $^{*}p < .01$ compared with the sham group; $^{\#}p < .05$, $^{\#\#}p < .01$ compared with the model group. (For interpretation of the references to color in this figure legend, the reader is referred to the web version of this article.)

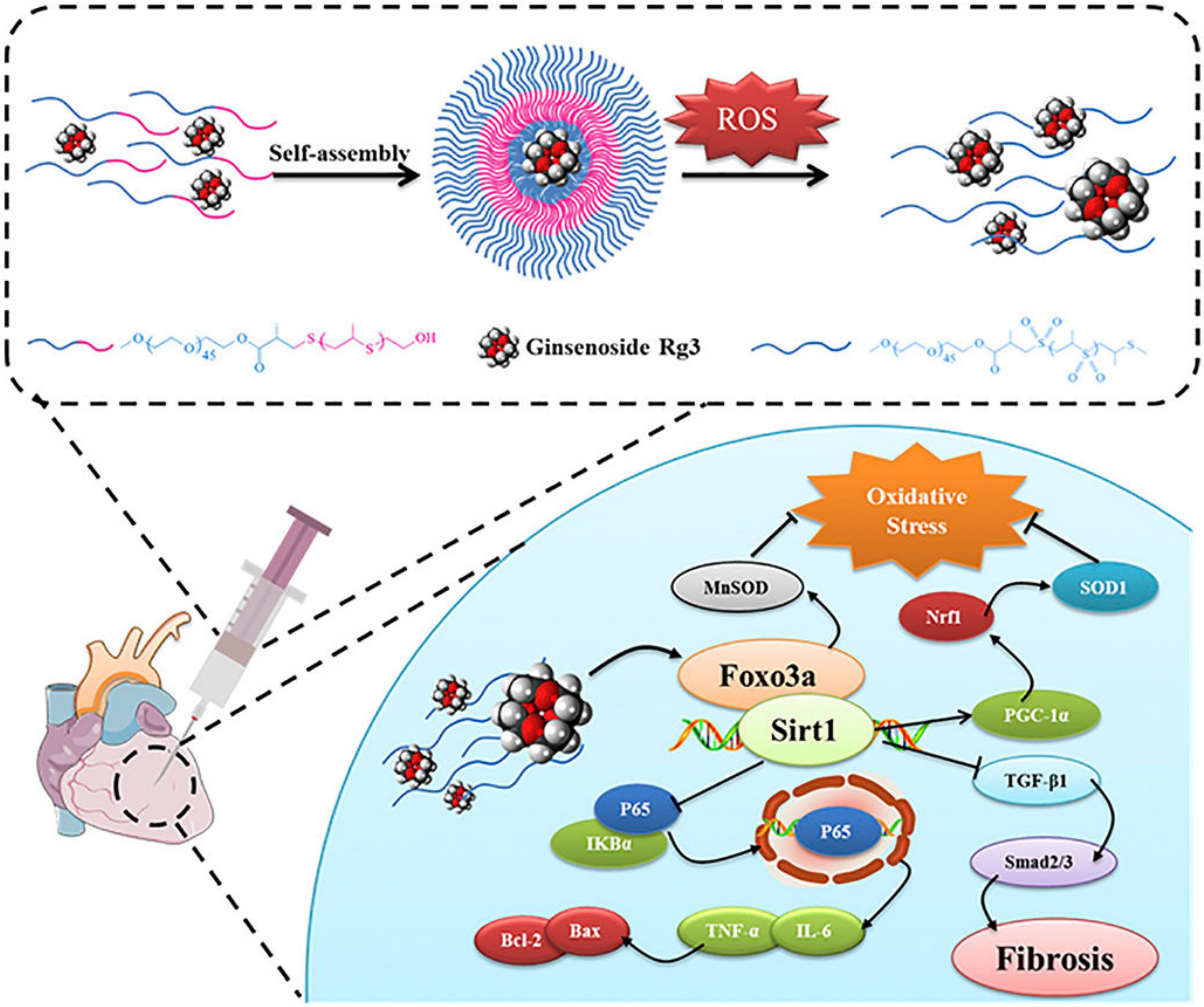

Fig. 9.

A schematic illustration showing that Rg3-loaded PEG-b-PPS nanoparticles responded to ROS, and the released Rg3 alleviated MIRI by interacting with FoxO3a, which had anti-oxidative, anti-inflammatory, and anti-fibrotic functions.